

Key words: X-rays: stars – stars: activity – stars: late-type

X-RAY ACTIVITY FROM DIFFERENT TYPES OF STARS

Lin He^{1,2}, Song Wang², Xiaojie Xu¹, Roberto Soria^{3,4,5}, Jifeng Liu^{2,3,6}, Xiangdong Li¹, Yu Bai², Zhongrui Bai², Jincheng Guo^{7,*}, Yanli Qiu^{2,3}, Yong Zhang⁸, Ruochuan Xu⁹, and Kecheng Qian¹⁰

- ¹ School of Astronomy and Space Science and Key Laboratory of Modern Astronomy and Astrophysics, Nanjing University, Nanjing, 210093, P. R. China
- ² Key Laboratory of Optical Astronomy, National Astronomical Observatories, Chinese Academy of Sciences, Beijing 100012, China; songw@bao.ac.cn
- ³ College of Astronomy and Space Sciences, University of Chinese Academy of Sciences, Beijing 100049, China
- ⁴ International Centre for Radio Astronomy Research, Curtin University, GPO Box U1987, Perth, WA 6845, Australia
- ⁵ Sydney Institute for Astronomy, School of Physics A28, The University of Sydney, Sydney, NSW 2006, Australia
- ⁶ WHU-NAOC Joint Center for Astronomy, Wuhan University, Wuhan, Hubei 430072, China
- ⁷ Department of Astronomy, Peking University, Beijing 100871, China
- ⁸ Nanjing Institute of Astronomical Optics & Technology, National Astronomical Observatories, Chinese Academy of Sciences, Nanjing 210042, China
- ⁹ International Department, the Affiliated High School of SCNU. No. 1 Zhongshandadao West, Tianhe District, Guangzhou 510630, China
- ¹⁰ United World College Changshu China. No.88 Kun-Cheng-Hu-Xi Road, Changshu, Jiangsu 215500, China

Abstract X-ray emission is an important indicator of stellar activity. In this paper, we study stellar X-ray activity using the *XMM-Newton* and LAMOST data for different types of stars. We provide a sample including 1259 X-ray emitting stars, of which 1090 have accurate stellar parameter estimations. Our sample size is much larger than those in previous works. We find a bimodal distribution of X-ray to optical flux ratio ($\log(f_X/f_V)$) for G and K stars. We interpret that this bimodality is due to two subpopulations with different coronal heating rates. Furthermore, using the full widths at half maxima calculated from H α and H β lines, we show that these stars in the inactive peaks have smaller rotational velocities. This is consistent with the magnetic dynamo theory that stars with low rotational velocities have low levels of stellar activity. We also examine the correlation between $\log(f_X/f_V)$ and luminosity

of the excess emission in the H α line, and find a tight relation between the coronal and chromospheric activity indicators.

1 INTRODUCTION

Stars of almost all stellar classes are X-ray emitters (Harnden et al., 1979; Stocke et al., 1983; Schmitt et al., 1995; Rogel et al., 2006). X-ray emission from late-type main-sequence stars comes from a magnetic corona which contains a plasma at temperature exceeding ~ 1 million K. The coronal magnetic structures and heating mechanisms are controlled by surface magnetic fields (Güdel, 2004), the latter of which are generally thought caused by a complex dynamo mechanism (e.g., Pizzolato et al., 2003).

The magnetic dynamo mechanism has been observationally evidenced by the famous activity-rotation correlation (Skumanich, 1972). Walter & Bowyer (1981) discovered the relation between X-ray luminosity (L_X) and rotation for RS CVn systems. A more accurate relation, $L_X \sim 10^{27}(V \sin i)^2$, was given by Pallavicini et al. (1981) for late-type stars. Furthermore, it was found that the activity-rotation correlation depends on the stellar mass (Pizzolato et al., 2003). This is explained as that the generation of magnetic energy by large-scale dynamo action is driven by rotation and convection (e.g., Charbonneau, 2010; Reiners et al., 2014). On the other hand, there is a saturated X-ray luminosity ($L_X/L_{\text{bol}} \approx 10^{-3}$, where L_{bol} is the bolometric luminosity) for most active stars where L_X/L_{bol} does not change below a certain rotation period (Vilhu, 1984; Vilhu & Walter, 1987). Two scenarios are often used to explain the saturation and super-saturation (i.e., the activity starts decreasing as stellar rotation rate increases to a critical value; Prosser et al., 1996) of stellar activity: polar up-drift migration (Solanki et al., 1997) and centrifugal stripping (Jardine & Unruh, 1999).

Although there have been many studies about stellar X-ray emission, some issues are still poorly understood, such as coronal heating and the evolution of stellar activity. One main limitation of previous studies is the small sample size of X-ray emitting stars with accurate stellar parameter estimations. This paper uses the largest spectral database, from observations by the Large Sky Area Multi-object Fiber Spectroscopic Telescope (LAMOST, also named the Guoshoujing Telescope), to present stellar parameters (e.g., effective temperature, surface gravity, metallicity) for more than 1200 X-ray emitting stars observed by *XMM-Newton*. We will study stellar X-ray activities over a wide range of stellar parameters. This may help us improve the understanding of these open issues (Testa et al., 2015).

The paper is organized as follows. In Section 2, we show the data analysis and sample selection from the 3XMM-DR5 (Rosen et al., 2016) and the LAMOST DR3 (Luo et al., 2015). In Section 3, we calculate the X-ray to optical flux ratio, and study the correlation between the X-ray to optical flux ratio and different stellar parameters. In Section 4, we discuss and explain the bimodality of stellar X-ray activity. Finally, we summarize the results in Section 5.

* LAMOST Fellow

2 SAMPLE SELECTION AND DATA REDUCTION

2.1 Sample Selection

We cross-matched the 3XMM-DR5 catalog and the LAMOST DR3 catalog using a radius of $3''$. This led to 3579 unique *XMM-Newton* sources with LAMOST spectral observations. To calculate the likelihood of mismatch, we shifted the positions of *XMM-Newton* sources by $1'$, and cross-matched them with the LAMOST catalog again using the same radius. In this case, we obtained 135 matches, and we conclude the likelihood of mismatch is about 3.77%.

We used several criteria to get a clean sample. Firstly, for the *XMM-Newton* data, we selected sources with `SUM_FLAG` ≤ 2 and `SC_EXTENT` = 0. The former is the summary flag derived from the EPIC warning flags, which is used to exclude spurious detections; the latter is the total band extent that is used to recognize point sources. Secondly, for the LAMOST spectra, we only used those with signal-to-noise ratio (SNR) higher than 7.5 in the r band. Thirdly, there are four main kinds of classes in the LAMOST database: “STAR”, “GALAXY”, “QSO”, and “Unknown”. Spectra flagged as “Unknown” were excluded from the sample. Some other sources, like double stars and white dwarfs, were also excluded according to the classification of the LAMOST catalog. This led to a sample of 1564 sources, including 134 Galaxies, 60 QSOs, and 1370 stars. Finally, we cross-matched the 1370 stars with the SIMBAD database using a radius of $3''$. About 100 sources are actually not main-sequence stars: 59 multiple objects, 32 pre-main-sequence stars, 18 globular clusters, one galaxy, and one possible active galactic nucleus (AGN). All these sources were excluded from the stellar sample. We visually checked all the spectra of the sample sources (e.g., stars, galaxies, and QSOs), and the final stellar sample contains 1259 stars.

2.2 LAMOST data

LAMOST is a reflecting Schmidt telescope with a clean aperture of 4 meters and a field of view of 5 degrees (Cui et al., 2012; Zhao et al., 2012). With 4000 fibers, it started its optical spectroscopic survey in 2012, and has successfully accomplished the fourth year mission (Deng et al., 2012; Luo et al., 2015). The third data release, DR3, contains 5,755,126 spectra, including 5,268,687 stellar spectra, 61,815 galaxy spectra, 16,351 spectra of quasars, and 408,273 spectra of unknown objects (Luo et al., 2015). In this work, we obtained the effective temperature (T_{eff}), metallicity ($[\text{Fe}/\text{H}]$), and surface gravity ($\log(g)$) from the stellar parameter catalogs for A-, F-, G-, and K-type stars. The typical uncertainties of the T_{eff} and $\log(g)$ are about 150 K and 0.3 dex (Wu et al., 2011). We collected the extinction estimations from Xiang et al. (2017); the typical uncertainty of $E(B - V)$ in their catalog is about 0.03. Finally, we calculated the equivalent width (EW) of the $\text{H}\alpha$ line, and the full width at half maximum (FWHM) of $\text{H}\alpha$ and $\text{H}\beta$ lines. The EW is calculated using the following formula:

$$\text{EW} = \int \frac{f(\lambda) - f(0)}{f(0)} d\lambda, \quad (1)$$

where $f(0)$ denotes the nearby pseudo-continuum flux.

2.3 XMM-Newton data

The 3XMM-DR5 catalog (Rosen et al., 2016) contains 565,962 X-ray detections comprising 396,910 unique X-ray sources, which is one of the largest X-ray source catalogues ever produced. We used PIMMS¹ to convert the 0.2–12 keV count rate (CR) to the unabsorbed 0.3–3.5 keV flux for the PN, M1, and M2, respectively. For stars we assumed an APEC model with individual absorptions, solar abundance, and a moderate coronal temperature ($\log T = 6.5$) for the stars (Schmitt et al., 1990). The individual absorptions for stars were converted from their extinctions (Foight et al., 2016),

$$N_H = (2.87 \pm 0.12) \times 10^{21} A_V \text{ cm}^{-2}. \quad (2)$$

The uncertainty of N_H is about $2.67 \times 10^{20} \text{ cm}^{-2}$. We should note that the unabsorbed X-ray flux f_X , converted from the count rate using PIMMS, is dependent on the coronal temperature set in the APEC model. However, the exact plasma temperature is not accurately known. To evaluate the influence on f_X , we re-estimated it with a higher temperature ($\log T = 7$). Using the mean value of N_H ($\approx 10^{21} \text{ cm}^{-2}$) for the sample stars, we find f_X decreases by a factor of ≈ 0.05 . Therefore, the influence of plasma temperature can be ignored in our study. For galaxies and QSOs we assumed a power-law model with $\Gamma = 1.7$ and Galactic foreground absorptions (Schlafly & Finkbeiner, 2011). Then, we obtained f_X as the mean value of the three cameras weighted by the errors. We used the EP_HR2 as the hardness ratio (HR), which is defined as $(\text{CR}_{1-2 \text{ keV}} - \text{CR}_{0.5-1 \text{ keV}}) / (\text{CR}_{1-2 \text{ keV}} + \text{CR}_{0.5-1 \text{ keV}})$ and calculated by averaging over all three cameras.

3 RESULTS

3.1 X-ray to optical flux Ratio

The ranges of X-ray to optical flux ratio are distinctly different for each stellar type, AGNs, BL Lac objects, clusters of galaxies, and normal galaxies (e.g., Stocke et al., 1991; Hornschemeier et al., 2003; Zickgraf et al., 2003; Brusa et al., 2007; Luo et al., 2008). Using the definition from Maccacaro et al. (1988), we estimated $\log(f_X/f_V)$ as

$$\log(f_X/f_V) = \log(f_X) + 0.4V_0 + 5.37, \quad (3)$$

where f_X is the unabsorbed 0.3–3.5 keV flux, and V_0 is the extinction-corrected V -band magnitude.

In order to obtain the V -band magnitude, we cross-matched the LAMOST DR3 catalog and the UCAC4 catalog (Zacharias et al., 2013) with a radius of $3''$. For objects without a UCAC4 V -band magnitude, we calculated it using the g and r magnitudes from the Sloan Digital Sky Survey (SDSS) following Jester et al. (2005):

$$V_0 = g_0 - 0.59 \times (g - r)_0 - 0.01. \quad (4)$$

The errors of $\log(f_X/f_V)$ were calculated as a combination of the errors of X-ray flux, V -band magnitude, and extinction. The X-ray information and the stellar parameters from the LAMOST catalog are summarized in Tables 1 and 2.

¹ <https://heasarc.gsfc.nasa.gov/docs/software/tools/pimms.html>

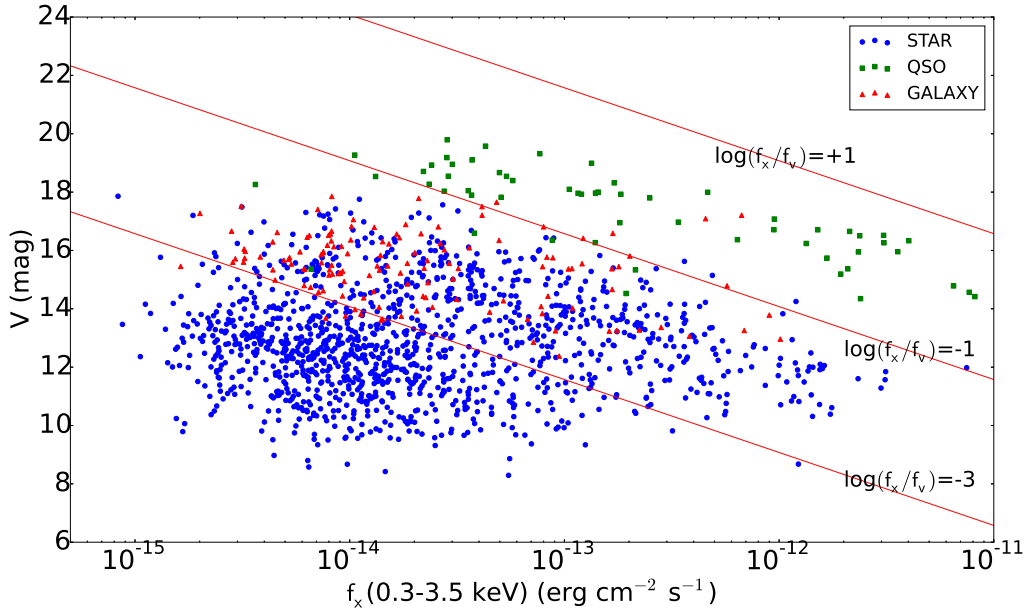


Fig. 1 V magnitude against f_X (0.3–3.5 keV). The blue, green, and red points indicate stars, QSOs, and galaxies, which are classified by the LAMOST catalog. The red lines indicate constant X-ray to optical flux ratios as +1, -1 and -3 .

3.2 $\log(f_X/f_V)$ for Stellar and Non-stellar Objects

Different kinds of objects have their typical ranges of $\log(f_X/f_V)$ values (Figure 1). Most of the stars have $\log(f_X/f_V)$ less than -1 ; most of the galaxies have $\log(f_X/f_V)$ between -3 and -1 ; most of the QSOs have $\log(f_X/f_V)$ between -1 and $+1$. These ranges are consistent with previous works (e.g., Stocke et al., 1991; Krautter et al., 1999; Georgakakis et al., 2004; Agüeros et al., 2009).

For the stellar sample, we divided these stars into four groups according to their spectral types. Each stellar type shows a widest range of emission levels, with $\log(f_X/f_V)$ ranging from ≈ -5 to ≈ -1 (Figure 2). Generally, late-type stars have higher $\log(f_X/f_V)$ than early-type stars, because the optical luminosity decreases more rapidly than the X-ray luminosity for decreasing stellar masses. The distributions of G and K stars show bimodality, which is consistent with previous studies (Stocke et al., 1991; Agüeros et al., 2009; Lin et al., 2012). For G stars, there are more inactive stars than active ones, while for K stars, more active stars are apparent. The $\log(f_X/f_V)$ distributions of K subtypes show clear bimodality (Figure 3). However, due to the sample limit, it is difficult to claim whether the G subtypes show bimodal distributions or broad distributions with local peaks. A clear evolutionary trend of the X-ray activity can be seen: from a single inactive distribution (F type), to a weak bimodal distribution (G type), to a clear bimodal distribution (K type), to a single active distribution (M type). Future work with a larger sample may shed more light on the distributions of the subtypes.

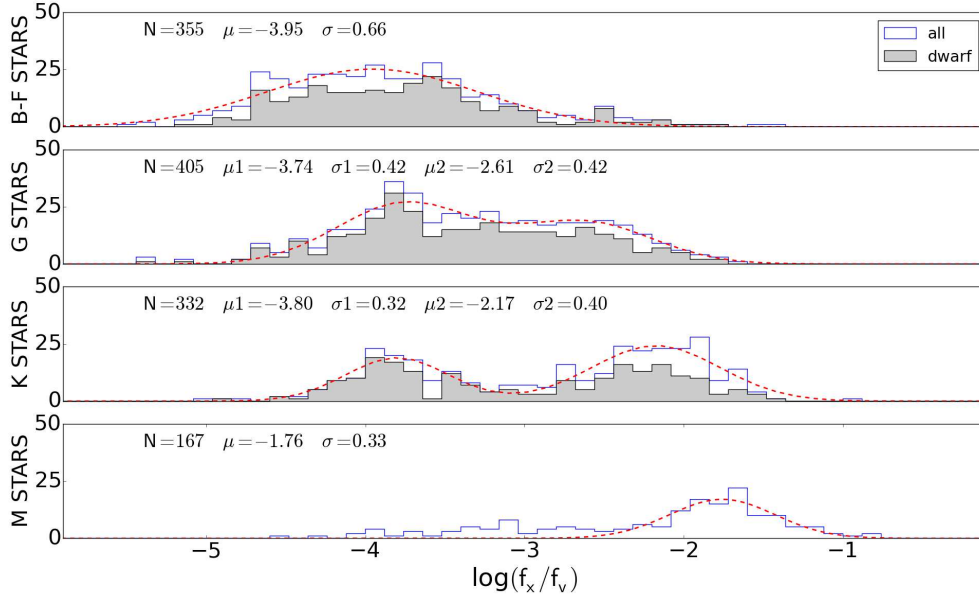


Fig. 2 $\log(f_X/f_V)$ distributions for B, A, F, G, K and M stars. The B, A and F groups are shown in one panel due to the small number of stars. The red dashed lines are the Gaussian fittings to the histograms. For the B-F and M groups, single-gaussian functions are used for the fitting, while for the G and K groups, double-gaussian functions are used to fit the $\log(f_X/f_V)$ distributions. The N , μ , σ indicate the number of sources, the mean value, and the standard deviation. Gray histograms represent the dwarfs in each spectral type. For B and M stars, no $\log(g)$ value was given by the LAMOST catalog, thus no giant and dwarf classification was done for them.

3.3 Comparison with Previous Works

Agüeros et al. (2009) calculated $\log(f_X/f_V)$ for 317 stars using the ROSAT All-Sky Survey (RASS; Voges et al., 1999) and the SDSS catalog. Figure 4 shows a comparison of the $\log(f_X/f_V)$ distribution between Agüeros et al. (2009) and our work. There are 124, 110, 67, and 15 stars in the F, G, K, and M types from Agüeros et al. (2009), respectively. In our work, there are two B stars, 36 A stars, 317 F stars, 405 G stars, 332 K stars, and 167 M stars.

Generally, the $\log(f_X/f_V)$ distributions of each spectral type in the two works are in good agreement. However, the distribution of K type stars in our sample shows more obvious double-peak structure than that of Agüeros et al. (2009). There are much less active K stars in Agüeros et al. (2009). This could be due to the energy limit (0.2–2.4 keV) of the *ROSAT* mission, which means that Agüeros et al. (2009) may have lost some of the sources with harder spectra that have higher $\log(f_X/f_V)$ values (Section 4.2). On the other hand, there are more inactive M stars in our sample. We propose this is due to a higher sensitivity of the *XMM-Newton* mission, therefore more sources with lower $\log(f_X/f_V)$ values can be detected.

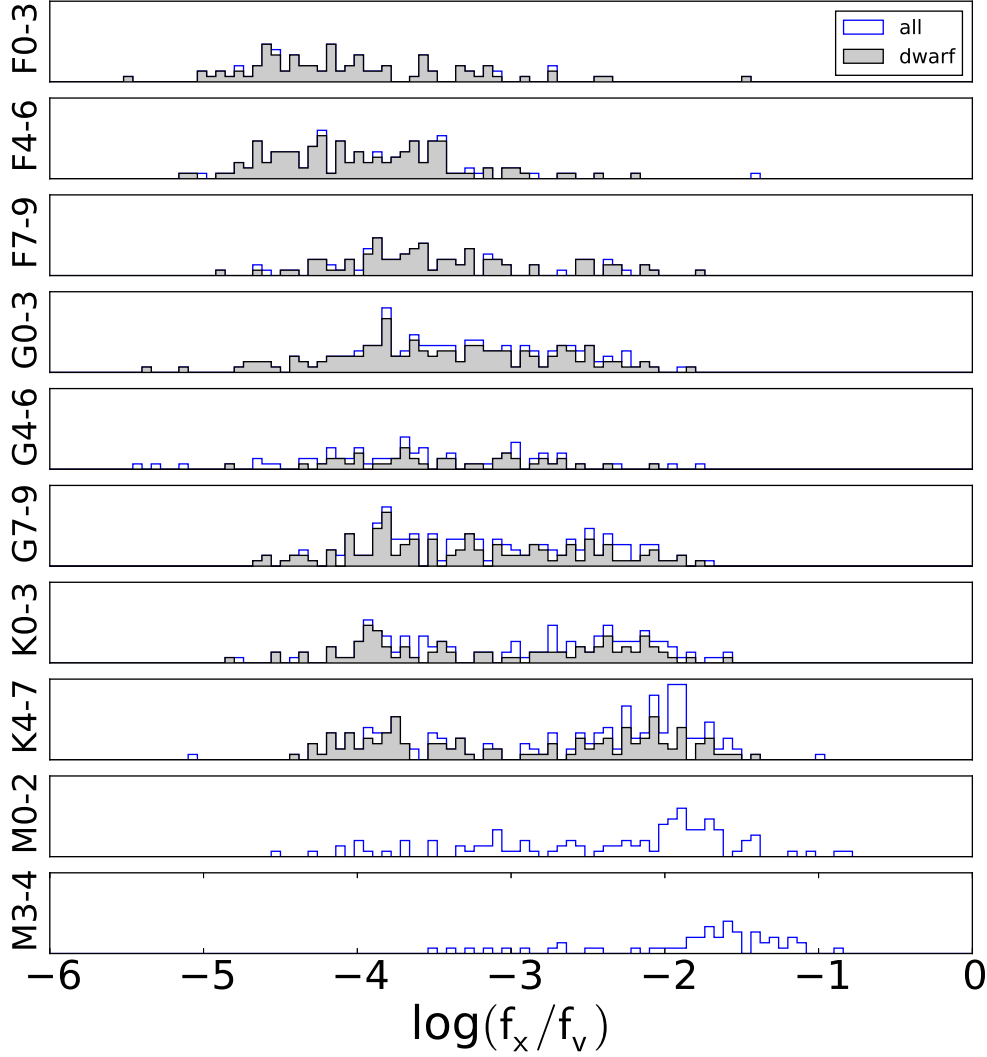


Fig. 3 $\log(f_X/f_V)$ distributions for subtypes of the F, G, K, and M stars. Gray histograms represent the dwarfs in each spectral type. For M stars, no $\log(g)$ value was given by the LAMOST catalog, thus no giant and dwarf classification was done for them.

3.4 Correlation Between $\log(f_X/f_V)$ and Stellar Parameters

Using stellar parameter estimations from LAMOST, we study the correlations between $\log(f_X/f_V)$ and stellar properties, including T_{eff} , $\log(g)$, $[\text{Fe}/\text{H}]$, and $\text{H}\alpha$ emission.

3.4.1 $\log(f_X/f_V)$ vs. T_{eff} and $\log(g)$

The bimodality of G- and K-type stars can also be seen in the $\log(f_X/f_V)$ - T_{eff} diagram (Figure 5). We divided the sources into two branches. For the primary branch, which contains the main part of the sources (outside the dashed rectangle), $\log(f_X/f_V)$ decreases with increasing temperature. This result is compatible with previous works (Stocke et al., 1991; Agüeros et al., 2009). For the

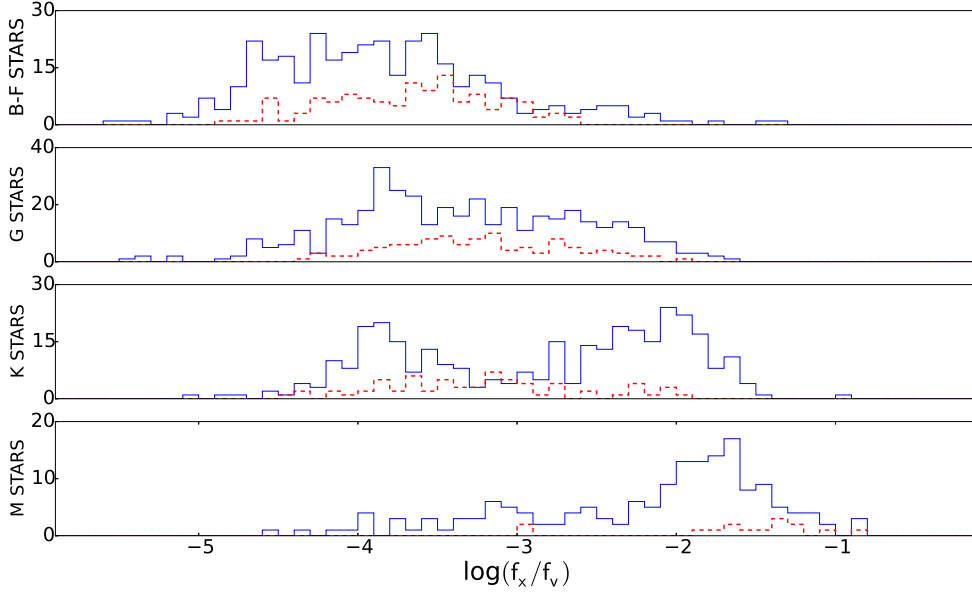


Fig. 4 Comparison of $\log(f_X/f_V)$ distributions for each spectral type in our sample and in Agüeros et al. (2009). The red dashed histograms show the sample from Agüeros et al. (2009), including 124, 110, 67 and 15 stars of the spectral types of F, G, K and M, respectively. The blue histograms show the distributions of our sample, including two B stars, 36 A stars, 317 F stars, 405 G stars, 332 K stars, and 167 M stars.

secondary branch (inside the blue dashed box), stars generally have constant low $\log(f_X/f_V)$ values for varying effective temperatures. The secondary branch is mainly constructed of cool stars ($T_{\text{eff}} < 5800$ K). We roughly defined a region for the secondary branch in the stellar parameter space: $3800 \text{ K} < T_{\text{eff}} \leq 5800 \text{ K}$; $-4.2 < \log(f_X/f_V) \leq -3.3$; $4.5 < \log(g) \leq 4.9$. The constraint on $\log(g)$ aims to exclude giant stars. The secondary branch contains most of the inactive G- and K-type stars, and it can be regarded as the inactive part of the two types stars. On the other hand, a group of stars ($3800 \text{ K} < T_{\text{eff}} < 5800 \text{ K}$; $\log(f_X/f_V) > -3.3$) in the primary branch can be considered as the active part of the G and K stars.

There are ≈ 108 giants showing X-ray emission, and some have high X-ray activity (Figure 6). This is consistent with previous studies that late-type giants can have (high) stellar activities (Simon & Drake, 1989; Aurière et al., 2015). However, some giants or sub-giants showing stellar activity may be in unrecognized binary systems (Özdarcan & Dal, 2018), and our data are not sufficient to associate the X-ray emission to the giants themselves or their unresolved dwarf companions (Schröder & Schmitt, 2007).

3.4.2 $\log(f_X/f_V)$ vs. $[Fe/H]$

There is no clear evidence for a correlation between X-ray activity and metallicity (Figure 7), however, for active stars ($\log(f_X/f_V) > -3$), a weak correlation between $\log(f_X/f_V)$ and $[Fe/H]$ is seen: more active stars are more metal-poor. This is consistent with Rocha-Pinto & Maciel (1998),

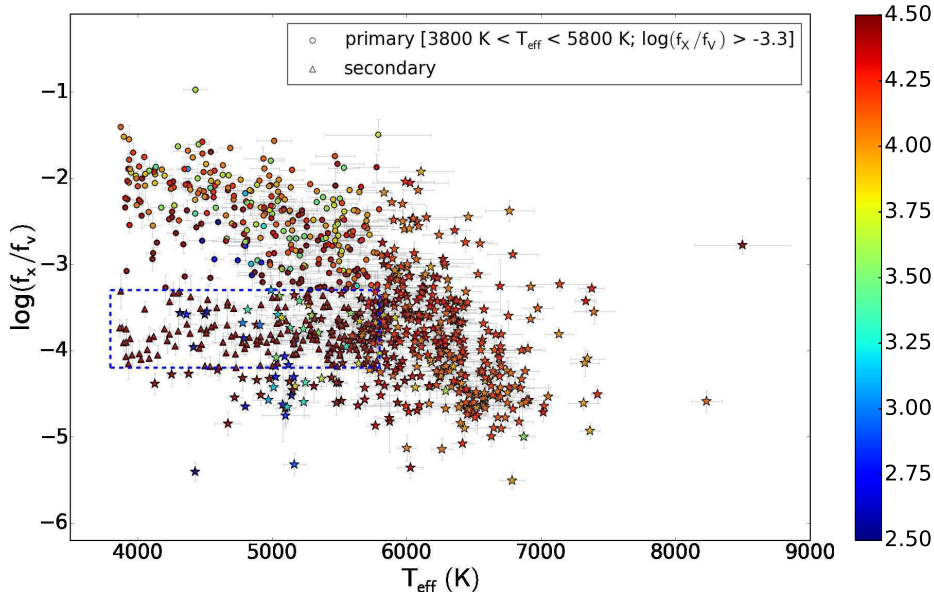


Fig. 5 $\log(f_X/f_V)$ as a function of temperature. The color shows different levels of $\log(g)$. The triangles inside the dashed rectangle mark the sources of the secondary branch. The circles represent the active part of the G and K stars in the primary branch, while the pentagrams represent the rest part of the primary branch.

who reported that the metallicities of very active stars are lower than those of normally active stars. Those inactive stars in the secondary branch are generally more metal-rich than the active stars (of the same spectral type) in the primary branch (Figure 8).

3.4.3 $\log(f_X/f_V)$ vs. $H\alpha$ Emission

Both the X-ray and $H\alpha$ emission are proxies of stellar magnetic activity (Testa et al., 2015), although they exist at different layers of the stellar atmosphere (i.e., corona and chromosphere). LAMOST in combination with XMM-Newton provide us with a great opportunity to study the relation between the two activity indicators. The EW of $H\alpha$ lines is listed in Table 3. Stars with positive EW, which means $H\alpha$ emission line, have higher $\log(f_X/f_V)$ values (Figure 9). All stars in the secondary branch (i.e., X-ray inactive) and most of the stars in the primary branch, which have low $\log(f_X/f_V)$ values, do not have $H\alpha$ excess emissions. As an example, the LAMOST spectra for two stars (one active and one inactive) are shown in Figure 10.

However, EW is not a suitable indicator of stellar activity since the continuum flux is very sensitive to the effective temperature (Reid et al., 1995; Yang et al., 2017). To remove the effects of effective temperature and surface gravity, we used the ratio of $H\alpha$ excess flux and bolometric flux to describe the activity of chromosphere. First, we constructed a “basal line” of $H\alpha$ emissions using those inactive stars in the secondary branch (Figure 11). The excess EW (hereafter EW’) is calculated by subtracting the basal value at the same temperature, i.e.,

$$EW' = EW - EW_{\text{basal}}. \quad (5)$$

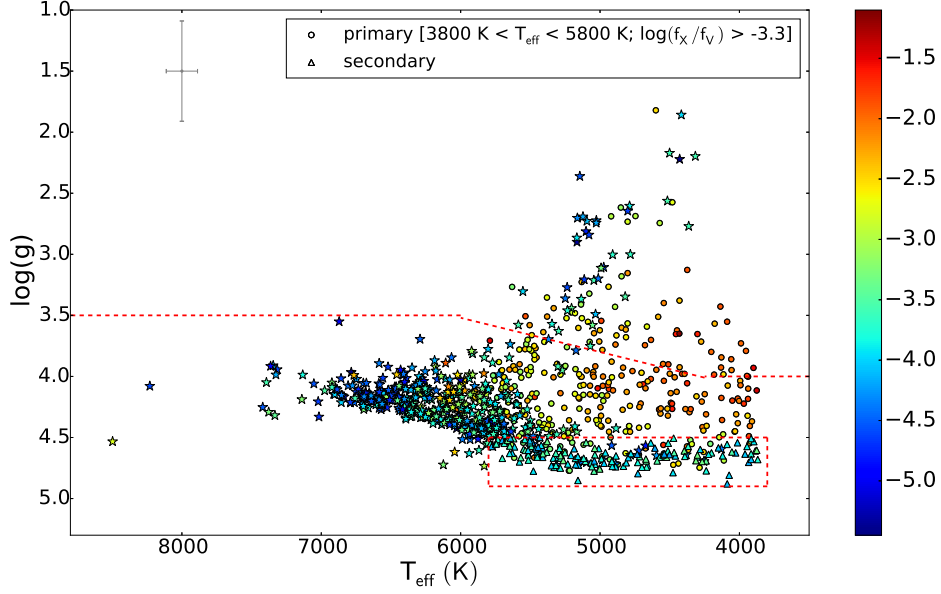


Fig. 6 $\log(g)$ as a function of temperature. The color shows different levels of $\log(f_X/f_V)$. The red dashed line is the separation between giant and dwarf stars (Ciardi et al., 2011). The meaning of the symbols is the same as in Figure 5.

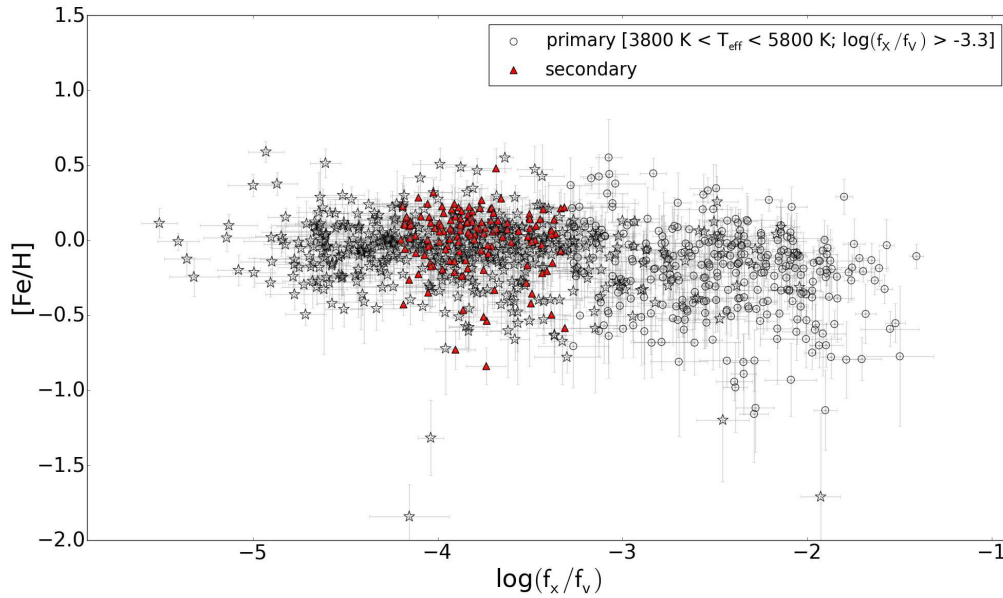


Fig. 7 Metallicity as a function of $\log(f_X/f_V)$. The meaning of the symbols is the same as in Figure 5.

Then, we calculated the stellar surface fluxes of $H\alpha$ emission lines ($f_{H\alpha}$) using the stellar atmosphere model CK04 (Castelli & Kurucz, 2004) based on the EW'. The CK04 models list physical fluxes of the spectra in unit of $\text{ergs cm}^{-2} \text{s}^{-1} \text{A}^{-1}$. For each star, the model with the most similar T_{eff} ,

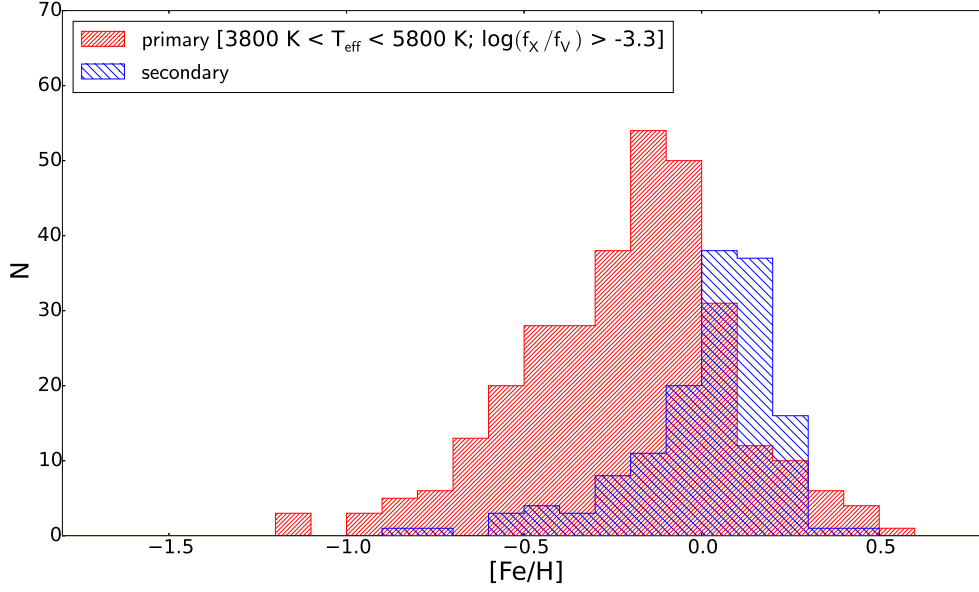


Fig. 8 Distribution of metallicities for stars in the primary and secondary branches.

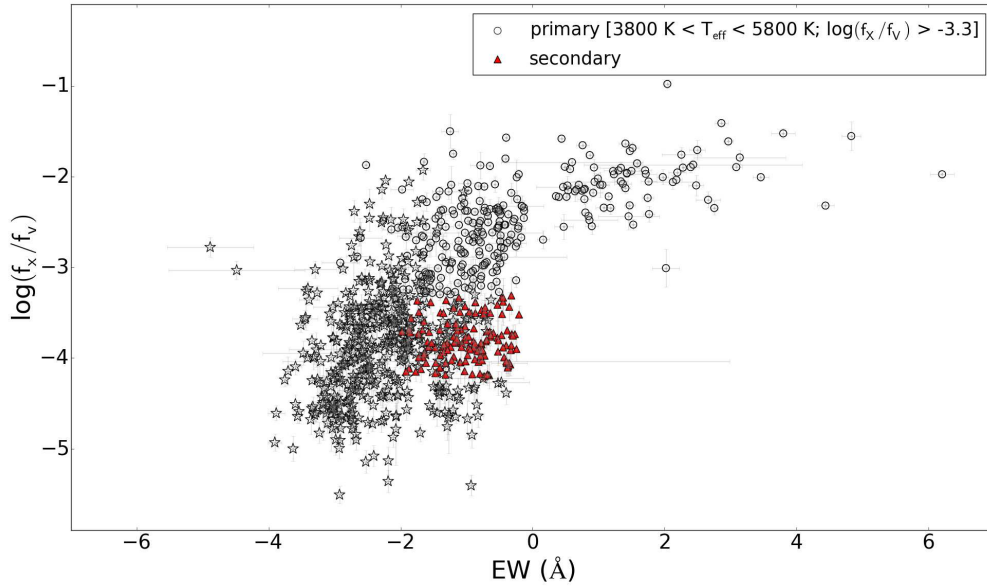


Fig. 9 $\log(f_X/f_V)$ as a function of the EW of the $H\alpha$ lines. The meaning of the symbols is the same as in Figure 5.

$\log g$, and $[\text{Fe}/\text{H}]$ was used. Finally, we determined the flux ratio $f_{H\alpha}/f_{\text{bol}}$ using the bolometric flux $f_{\text{bol}} = \sigma T^4$, with the stellar temperature from LAMOST. A power law dependence of f_X/f_V on $f_{H\alpha}/f_{\text{bol}}$ (Figure 12) is determined as,

$$\log(f_X/f_V) = (1.21 \pm 0.23) \times \log(f_{H\alpha}/f_{\text{bol}}) + (2.53 \pm 0.87). \quad (6)$$

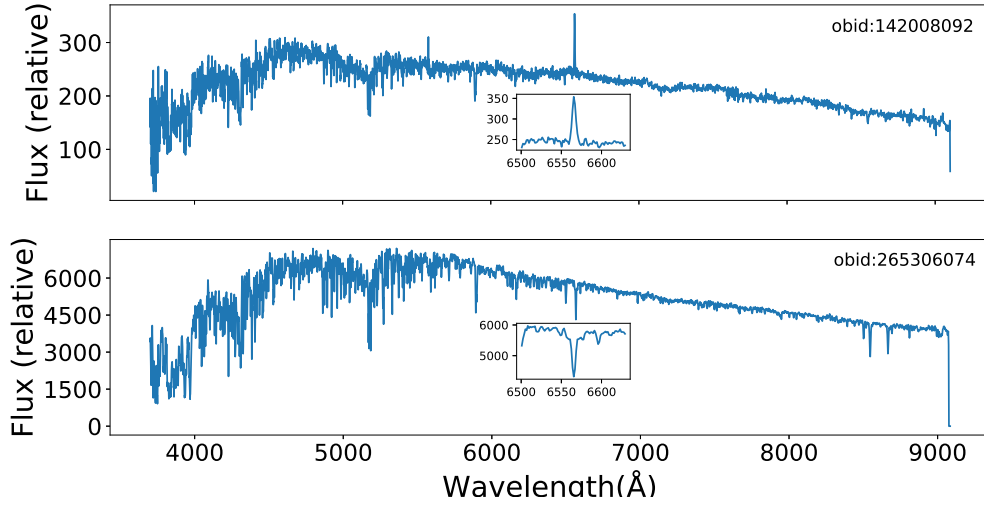


Fig. 10 Examples of LAMOST spectra for one active star (top panel) and one inactive star (bottom panel). The subplots show the $H\alpha$ lines.

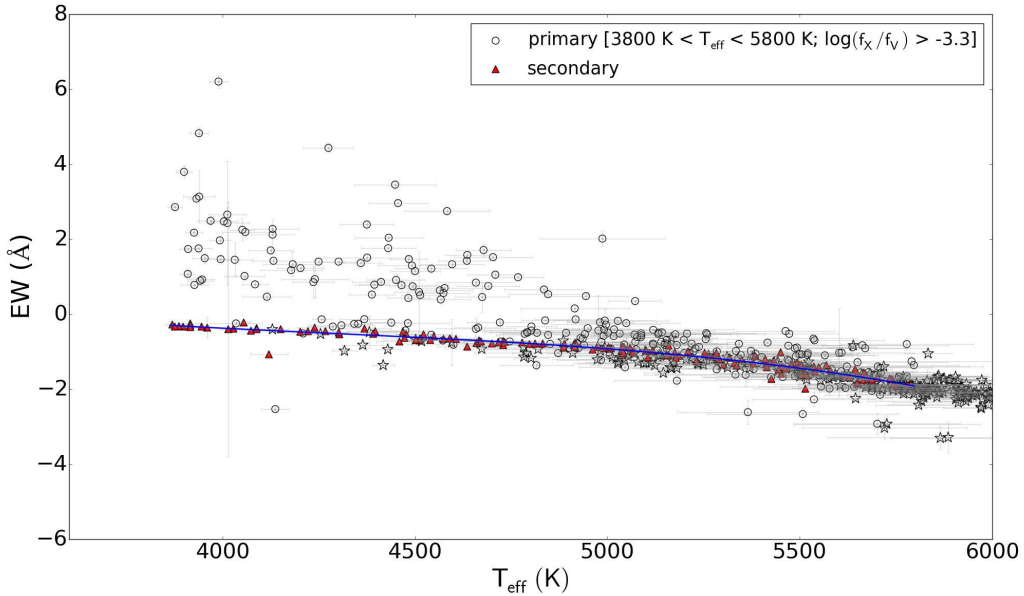


Fig. 11 $EW_{H\alpha}$ as a function of T_{eff} . The meaning of the symbols is the same as in Figure 5. The solid line is the fitted “basal line” using the inactive stars in the secondary branch.

Recently, Martínez-Arnáiz et al. (2011) reported a relation between X-ray and $H\alpha$ emission as $F_X \propto F_{H\alpha}^{1.48 \pm 0.07}$, using a sample of late-type dwarf active stars with spectral types from F to M. For M dwarfs, Stelzer et al. (2013) derived $L_X/L_{\text{bol}} \propto (f_{H\alpha}/f_{\text{bol}})^{1.90 \pm 0.31}$. In our study, we have obtained that $f_X/f_V \propto (f_{H\alpha}/f_{\text{bol}})^{1.12 \pm 0.30}$, a slightly flatter relation than found in those other studies. The discrepancy may be due to our small sample size. In addition, we should note that the lack of simultaneous observations of those two intrinsically varying properties (coronal

and chromospheric activities) may introduce another source of uncertainty in all these studies (Martínez-Arnáiz et al., 2011).

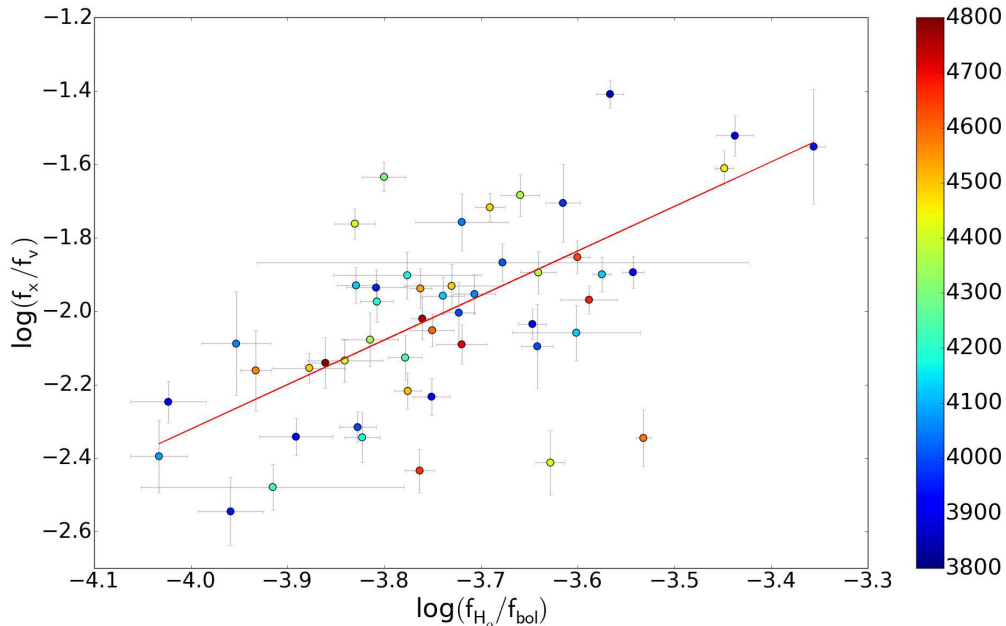


Fig. 12 $\log(f_X/f_V)$ as a function of $\log(f_{H\alpha}/f_{bol})$. The color shows different effective temperatures. The red line corresponds to the relationship $\log(f_X/f_V) = (1.21 \pm 0.23) \times \log(f_{H\alpha}/f_{bol}) + (2.53 \pm 0.87)$.

4 THE BIMODALITY OF X-RAY ACTIVITY

The $\log(f_X/f_V)$ distributions of G and K stars show clear bimodality (See Figure 2 and 5). The gap between the peaks of the bimodal distribution is similar to that discovered by Vaughan & Preston (1980) using the Ca II H&K lines. That gap was first explained as a sudden change of dynamo activity to a less efficient mode at a critical rotation rate, but the scenario was rejected because the dependence of the chromospheric emission on rotation and spectral type is the same for stars above and below the gap (Noyes et al., 1984). Other studies with Ca II H&K, $H\alpha$, and X-ray emission have also found the bimodality of stellar activity, with an active and inactive peak (e.g., Henry et al., 1996; Wright et al., 2004; Jenkins et al., 2011; Martínez-Arnáiz et al., 2011; Pace, 2013). The bimodality is now explained as one young and one old subpopulation. The old one is often thought to be inactive in chromospheric and X-ray emission, since the magnetic activity decreases simultaneously as the rotation decelerates with age (e.g., Mamajek & Hillenbrand, 2008; Katsova & Livshits, 2011).

The sky distribution (Figure 13) shows no obvious distinction of the stars in the two branches. That means those two branches are not belonging to different local structures (e.g., stellar streams). Before we discuss the bimodality of X-ray activity, we firstly checked the possibility that the bimodality is caused by selection effects, i.e., whether the detection limitations of *XMM-Newton*

and LAMOST can produce a double-peaked distribution from a single-peaked f_X and a single-peaked V distribution.

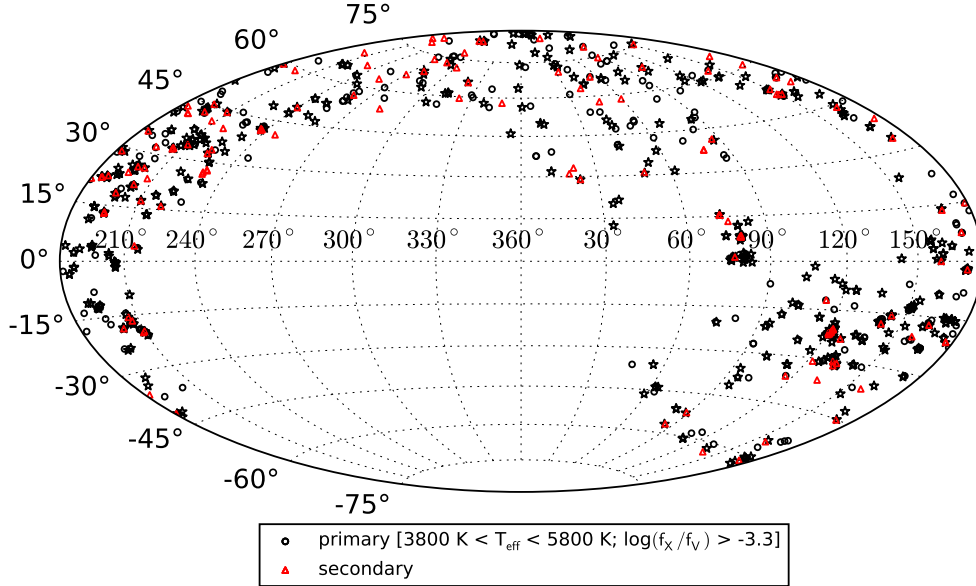


Fig. 13 The sky distribution of our stellar sources in Galactic coordinations. The meaning of the symbols is the same as in Figure 5.

4.1 Selection Effect

We performed a Monte Carlo simulation to check whether the bimodality is caused by selection effects. The detailed steps are as follows:

- (i) We simulated a sample including 10 million sources with different effective temperatures, using the proportion from the LAMOST stellar parameter catalogs.
- (ii) We obtained the relation between $\log(f_X/f_V)$ and temperature by fitting to the observed distribution of the primary branch as,

$$\log(f_X/f_V) = (-9.05 \pm 0.33) \times 10^{-4}T + (1.99 \pm 0.19). \quad (7)$$

Using this Equation, we calculated $\log(f_X/f_V)$ values for the 10 million simulated sources.

- (iii) We obtained the relation between absolute magnitude and temperature by fitting the data in Wegner (2007), using a cubic polynomial equation as,

$$M_V = (-7.19 \pm 5.69) \times 10^{-12}T^3 + (4.0 \pm 1.09) \times 10^{-7}T^2 - (57.6 \pm 6.74) \times 10^{-4}T + (25.5 \pm 1.32). \quad (8)$$

Using this Equation, we calculated the absolute magnitudes for the simulated sources (Figure 14, top left panel).

- (iv) We derived the relation between X-ray luminosity and temperature using Equation 7 and 8, following,

$$\log(L_X/L_V) = \log(f_X/f_V), \quad (9)$$

and

$$\log(L_V) = -0.4 \times (M_V - M_{\odot,V}) - \log(L_{\odot,V}). \quad (10)$$

The absolute magnitude and luminosity for the Sun is 4.85 mag (Worthey et al., 1994) and 4.64×10^{32} erg s⁻¹. We then obtained the X-ray luminosities for the simulated stars (Figure 14, bottom left panel).

(v) Assuming the stars are located in the Galaxy, we assigned random distances (from 1 pc to 15 kpc; Amôres et al., 2017)) to each star (Figure 14, top right panel).

(vi) We calculated the apparent magnitude and X-ray flux using the simulated M_V , L_X , and distance D . The detection limits were set for LAMOST ($10 < V < 20$) and *XMM-Newton* (10^{-15} erg s⁻¹ $< f_X < 10^{-11}$ erg s⁻¹) to select simulated sources that can be detected.

(vii) We re-calculated the $\log(f_X/f_V)$ with Equation 3, using the apparent magnitude and X-ray flux. The simulated distribution is shown in Figure 14 (bottom right panel).

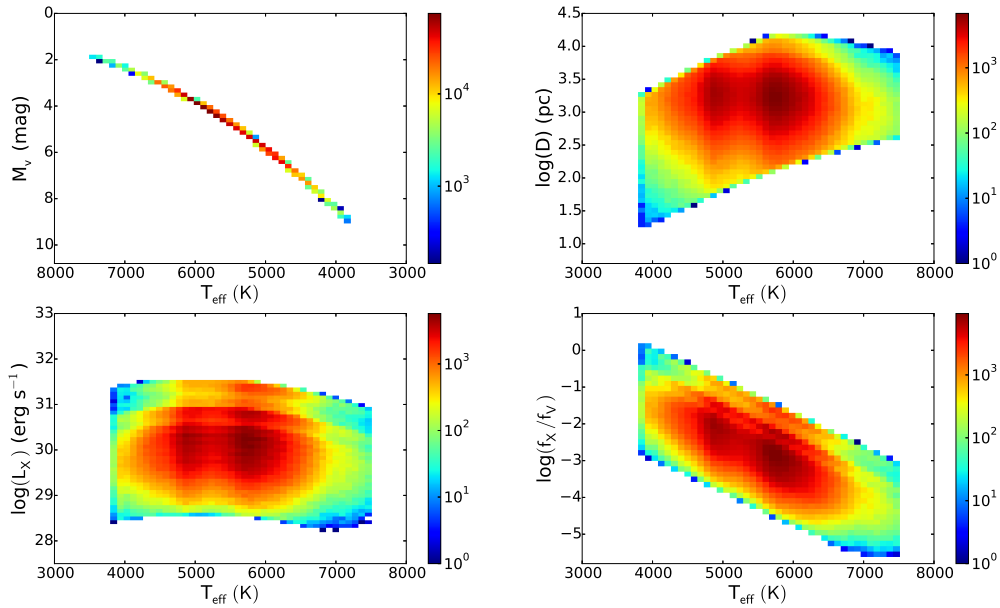


Fig. 14 Distributions of the parameters from the simulated sample. The color indicates the numbers of simulated sources. Top left panel: absolute magnitude as a function of temperature for the simulated sources. Bottom left panel: X-ray luminosity as a function of temperature for the simulated sources. Top right panel: distance as a function of the temperature for the simulated sources. Bottom right panel: X-ray to optical flux ratio as a function of temperature for the simulated sources.

The simulated distributions of M_V , L_X , and $\log(f_X/f_V)$ for G and K stars are plotted in Figure 15. The simulated single-peaked distributions of $\log(f_X/f_V)$ mean that the observed bimodality of G and K stars (Figure 2) is not due to selection effect.

² <http://astro.pas.rochester.edu/aquillen/ast142/costanti.html>

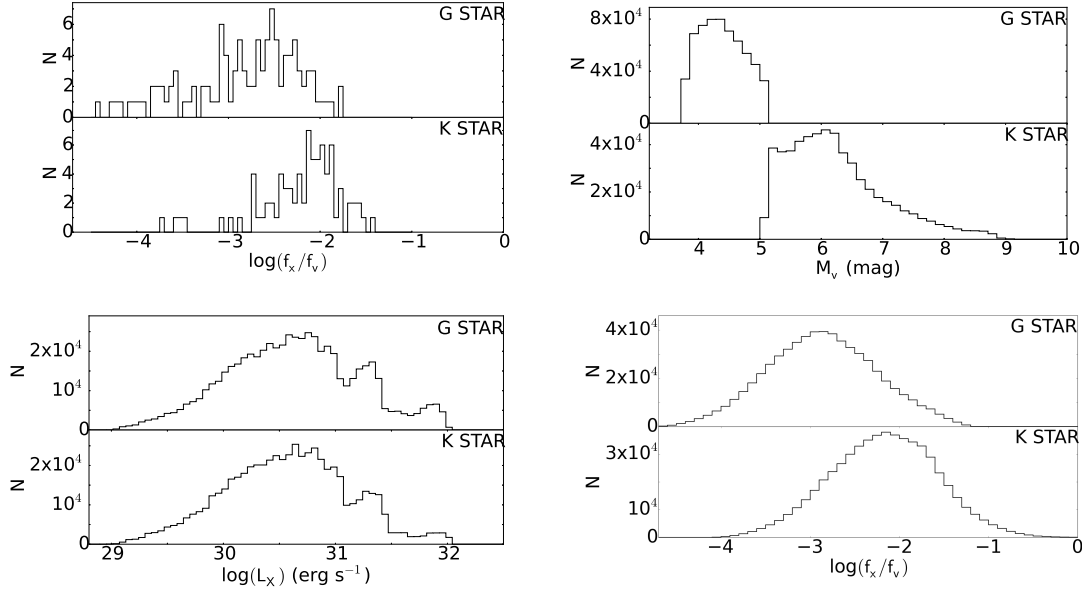


Fig. 15 Histograms of some parameters for G and K stars. Top left panel: The observed $\log(f_X/f_V)$ distributions of G and K stars in the primary branch. Top right panel: The M_V distributions for the simulated G and K stars. Bottom left panel: The L_X distributions for the simulated G and K stars. Bottom right panel: The $\log(f_X/f_V)$ distributions of the simulated G and K stars.

4.2 Hardness Ratio

The coronal temperature is known to be positively correlated with X-ray luminosity and stellar activity (e.g., Vaiana, 1983; Schrijver et al., 1984; Schmitt, 1997; Güdel, 2004; Jeffries et al., 2006; Telleschi et al., 2005, 2007). The cause of this relation between coronal temperature and luminosity can be that they are both functions of magnetic activity (Güdel, 2004). A more efficient dynamo inside active stars (for example because of faster rotation) produces stronger magnetic fields in the corona, and consequently a higher rate of field line reconnections and flares. This results both in a larger density of energetic electrons in the corona, and in higher temperatures. Therefore, we suggest that the double-peaked distribution of $\log(f_X/f_V)$ represents a double-peaked distribution of heating rates, and therefore coronal temperatures.

In our work, we take the X-ray HR as a proxy for the coronal temperature, because hotter corona will emit photons with higher energies, which produces harder X-ray spectra. There is a positive correlation between $\log(f_X/f_V)$ and HR (Figure 16). That means stronger X-ray emitters (higher $\log(f_X/f_V)$) have higher coronal temperatures. To have a better look, we classified the objects into three types: hard, median, soft sources, using the criteria as: hard ($0.3 < HR < 1$), median ($-0.6 < HR < 0.3$), and soft ($-1 < HR < -0.6$). We find (Figure 17) that (1) the higher activity peak of the $\log(f_X/f_V)$ distribution in G-type stars is dominated by hard sources, and the lower activity peak by median and soft sources; (2) the higher activity peak of the $\log(f_X/f_V)$

distribution in K-type stars is dominated by hard and median sources, and the lower activity peak by soft sources.

Besides G and K stars, the bimodality was also detected in late F and early M stars (Section 3.2), although the statistics are too poor due to the sample limit. One question is that why the bimodality is not detected for those hotter or cooler stars. For hotter stars (early F and earlier), the coronal heating efficiency may be quite low for most of them. For cooler stars (late M), firstly, they are generally optically faint, thus our sample may be not complete; secondly, stars later than M4 type may have different dynamo mechanism due to their fully convective feature (Durney et al., 1993); thirdly, the evolution of M stars is very slow, which means most of them are still in the regime with high coronal heating rate. In fact, most of the M stars have high HR values around 0 (Figure 16).

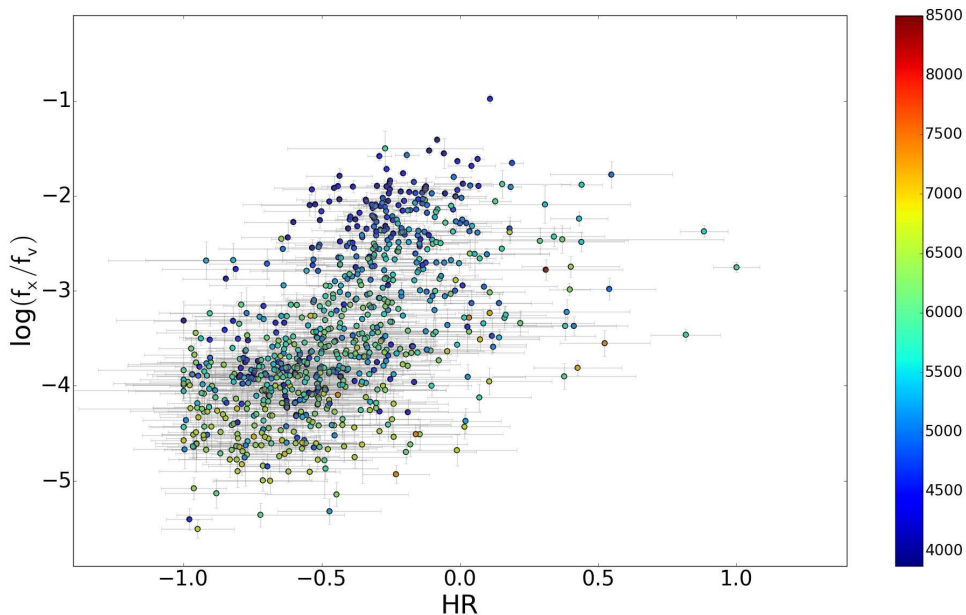


Fig. 16 $\log(f_X/f_V)$ as a function of HR. The color shows different effective temperatures.

4.3 Rotational Velocities

The magnetic dynamo suggests a lower rotation velocity for inactive stars than active ones. Therefore, we further checked the difference of rotational velocities of the primary branch ($3800 \text{ K} < T_{\text{eff}} < 5800 \text{ K}$; $\log(f_X/f_V) > -3.3$) and secondary branch. They can be regarded as the active and inactive parts (of G and K stars), respectively. In our work, we take the FWHMs of Balmer lines as proxies of rotational velocities (Strassmeier et al., 1990; Fekel, 1997).

The instrumentally corrected FWHM is calculated as

$$\text{FWHM}_{\text{cor}} = (\text{FWHM}_{\text{obs}}^2 - \text{FWHM}_{\text{inst}}^2)^{1/2}, \quad (11)$$

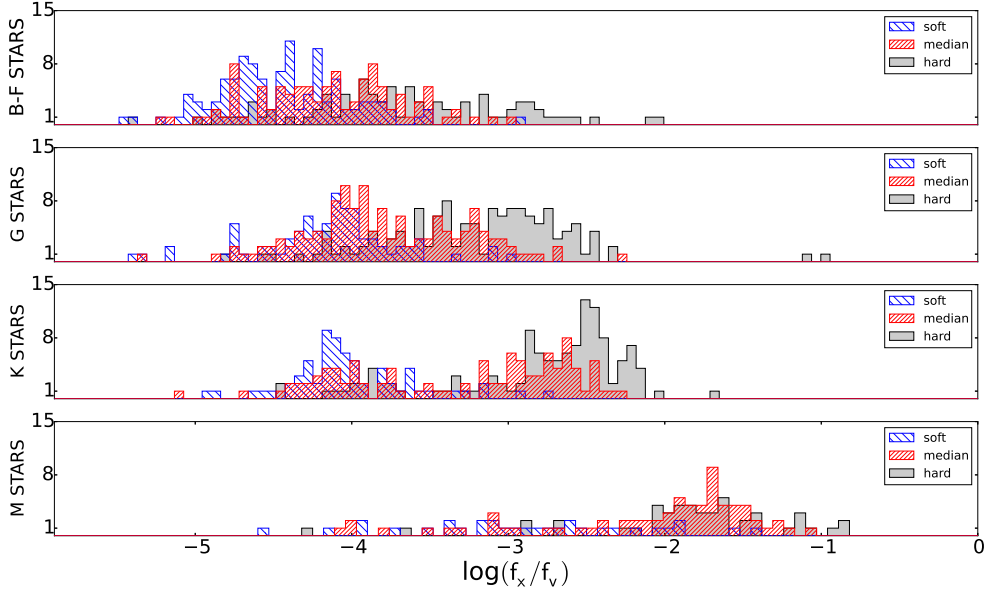


Fig. 17 Distribution of $\log(f_X/f_V)$ for three types with different HR : hard ($0.3 < HR < 1$), median ($-0.6 < HR < 0.3$), and soft ($-1 < HR < -0.6$). It is clear that hard sources have the highest $\log(f_X/f_V)$ values, while soft sources have the lowest values. The mean $\log(f_X/f_V)$ values of the soft, median, and hard sources in the G type are -3.93 , -3.48 , and -2.81 , and their spread around the mean $\log(f_X/f_V)$ are 0.53 , 0.61 , and 0.69 , respectively. The mean $\log(f_X/f_V)$ values of the three kinds of sources in the K type are -3.75 , -2.91 , and -2.33 , and their spread around the mean $\log(f_X/f_V)$ are 0.48 , 0.8 , and 0.67 , respectively.

where FWHM_{obs} is the observed FWHM, $\text{FWHM}_{\text{inst}}$ the FWHM of the lamp lines, and FWHM_{cor} the corrected FWHM (Strassmeier et al., 1990). Here we calculated the FWHMs of $H\alpha$ and $H\beta$ lines, for 540 and 596 stars, respectively (Table 3). Collisional broadening and broadening as a result of macro-turbulence were not corrected for. The corrected FWHMs measured from $H\alpha$ and $H\beta$ lines are in good agreement (Figure 18). The mean deviation between the FWHMs from the two lines is $\approx 0.43 \text{ \AA}$, with a standard deviation as $\approx 1.09 \text{ \AA}$.

The FWHMs of the secondary branch stars are generally smaller than those of the part of primary branch stars (Figure 19), indicating relatively lower rotational velocities of the secondary branch sources. This further explains the bimodality of the X-ray activity of G and K stars. Low rotational velocity weakens the coronal activity (Pallavicini et al., 1981; Pizzolato et al., 2003; Wright et al., 2011) and, therefore the X-ray to optical flux ratio.

5 CONCLUSION

The *XMM-Newton* and LAMOST data allow us to identify X-ray emitters and probe stellar X-ray activity over a wide range of stellar parameters. By cross matching the 3XMM-DR5 catalog and the LAMOST DR3 catalog, we provide a sample including 1259 X-ray emitting stars, of which

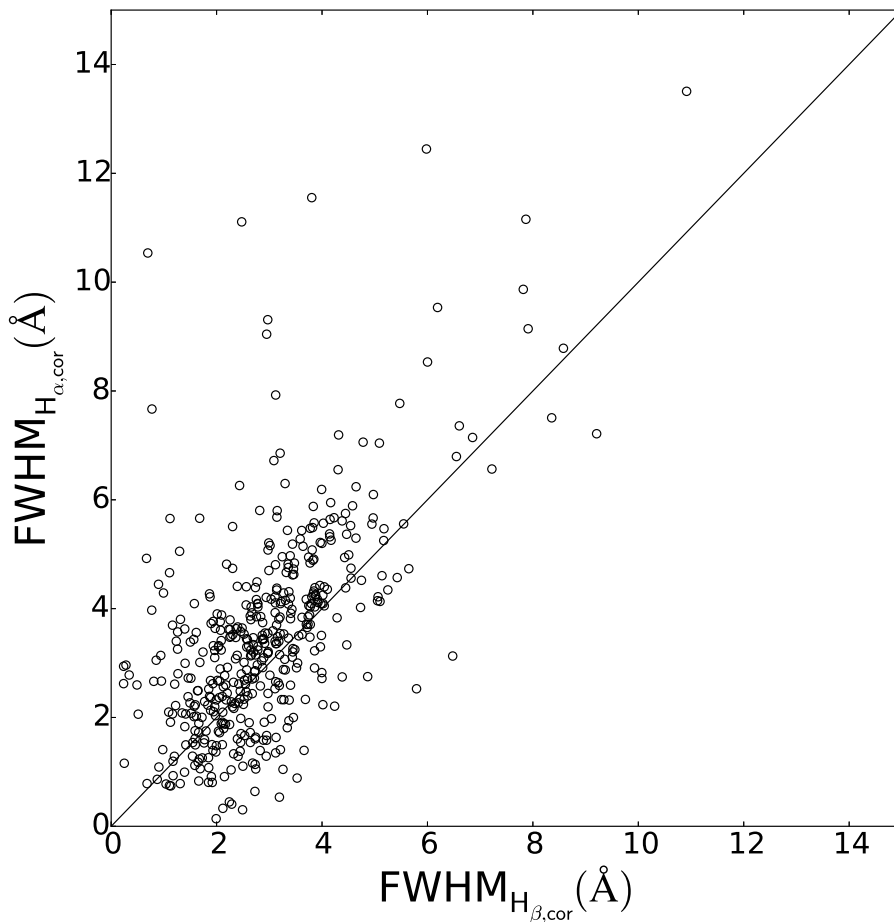


Fig. 18 Comparison of corrected FWHMs calculated from $H\alpha$ and $H\beta$ lines.

1090 have accurate stellar parameter estimations. Our sample size is much larger than those in previous works. We studied the X-ray emission level, using X-ray to optical flux ratio, for different stellar types, including two B stars, 36 A stars, 317 F stars, 405 G stars, 332 K stars, and 167 M stars. Late type stars in general have higher $\log(f_X/f_V)$ values than early type ones, indicating their higher X-ray activity.

We find a bimodal distribution of $\log(f_X/f_V)$ for G- and K-type stars. We performed a Monte Carlo simulation which proves that the double-peaked distribution are not caused by selection effect. We explain this bimodality as evidence of two subpopulations with different coronal heating rates, and therefore different coronal temperatures. Stars with a hotter corona — observationally with a higher HR — have a higher X-ray $\log(f_X/f_V)$ value. Furthermore, we calculated the FWHMs of $H\alpha$ and $H\beta$ lines, and found that those inactive stars have generally smaller FWHMs, and therefore lower rotational velocities, than active stars. In fact, the $\log(f_X/f_V)$ distributions of the late F and early M types also display weak bimodality, but the statistics are very poor due to the sample limit. Future studies with more F and M stars may shed more light on the distribution. In general, the rotation velocity and stellar activity observationally decay with stellar age (e.g., Wilson,

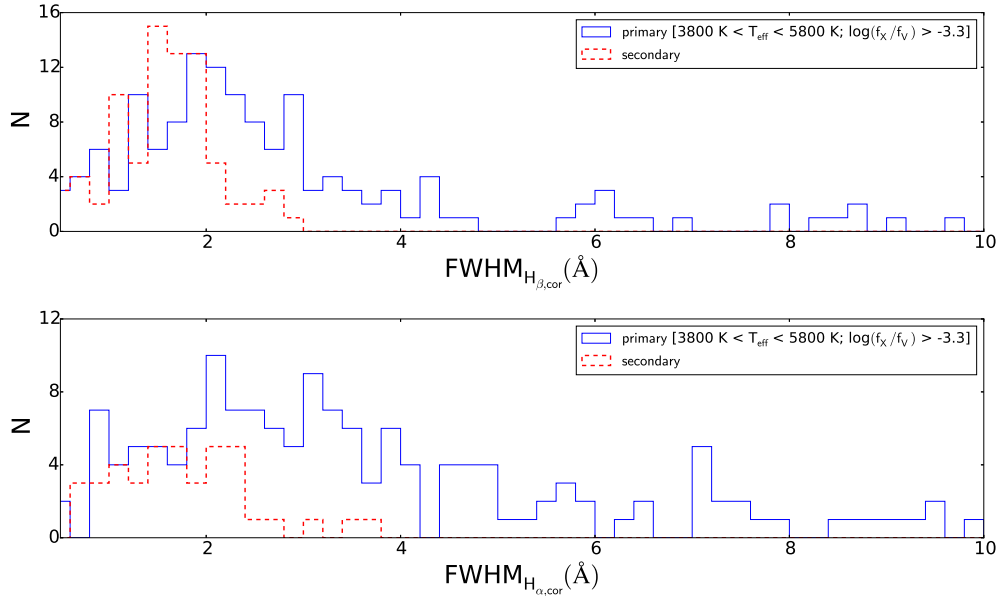


Fig. 19 Top panel: distributions of corrected FWHMs calculated from $H\beta$ lines for the primary and secondary branch. Bottom panel: distributions of corrected FWHMs calculated from $H\alpha$ lines for the primary and secondary branch.

1963; Skumanich, 1972; Simon et al., 1985; Cardini & Cassatella, 2007; Mamajek & Hillenbrand, 2008), therefore, those inactive stars with much higher $\log(g)$ values are possibly old stars. We speculate that the old age, stellar activity cycles like those displayed by the sun (Judge et al., 2003), and long-term variation (such as Maunder minimum: Baliunas & Jastrow, 1990; Henry et al., 1996) may all contribute to the inactive part. We also examined the correlation between $\log(f_X/f_V)$ and $H\alpha$ emission line luminosity, and find a positive tight correlation between the two quantities.

Acknowledgements This research has made use of data obtained from the 3XMM XMM-Newton serendipitous source catalogue compiled by the 10 institutes of the XMM-Newton Survey Science Centre selected by ESA. Guoshoujing Telescope (the Large Sky Area Multi-Object Fiber Spectroscopic Telescope LAMOST) is a National Major Scientific Project built by the Chinese Academy of Sciences. Funding for the project has been provided by the National Development and Reform Commission. LAMOST is operated and managed by the National Astronomical Observatories, Chinese Academy of Sciences. We acknowledge use of the SIMBAD database and the VizieR catalogue access tool, operated at CDS, Strasbourg, France, and of Astropy, a community-developed core Python package for Astronomy (Astropy Collaboration, 2013). We are grateful for support from the National Science Foundation of China (NSFC, Nos. 11273028, 11333004, 11603035, 11603038, and 11503054). RS acknowledges support from a Curtin University Senior Research Fellowship; he is also grateful for support, discussions and hospitality at the Strasbourg Observatory during part of this work.

Table 1 The X-ray information for the sample sources.

obsid	f_x	$\log(f_x/f_V)$	HR
	($\text{erg s}^{-1} \text{cm}^{-2}$)		
(1)	(2)	(3)	(4)
1603040	$9.67\text{e-}15\pm 1.71\text{e-}15$	-2.51 ± 0.14	0.57 ± 1.11
7003074	$5.06\text{e-}14\pm 4.81\text{e-}15$	-1.93 ± 0.06	0.23 ± 0.44
7003243	$5.11\text{e-}15\pm 6.01\text{e-}16$	-2.78 ± 0.07	-1.00 ± 2.41
7711046	$3.72\text{e-}14\pm 3.63\text{e-}15$	-2.14 ± 0.06	-1.00 ± 0.35
20001189	$5.74\text{e-}14\pm 1.86\text{e-}15$	-1.49 ± 0.04	-0.36 ± 0.06
28306100	$5.44\text{e-}15\pm 8.75\text{e-}16$	-3.89 ± 0.08	-0.89 ± 1.00
51007061	$1.68\text{e-}14\pm 1.37\text{e-}15$	-3.80 ± 0.05	-1.00 ± 0.90
53111238	$2.26\text{e-}14\pm 2.53\text{e-}15$	-4.12 ± 0.06	-0.93 ± 1.66
74309103	$1.69\text{e-}14\pm 1.78\text{e-}15$	-4.61 ± 0.09	-1.00 ± 0.53
74311158	$3.54\text{e-}14\pm 2.38\text{e-}15$	-4.19 ± 0.08	-0.91 ± 0.43
74403036	$1.74\text{e-}14\pm 1.10\text{e-}15$	-3.64 ± 0.05	-0.55 ± 0.29
75805212	$3.10\text{e-}14\pm 1.48\text{e-}15$	-2.42 ± 0.05	-0.69 ± 0.13
76406132	$2.17\text{e-}14\pm 2.01\text{e-}15$	-4.43 ± 0.05	-0.82 ± 0.40
76506084	$1.29\text{e-}14\pm 1.32\text{e-}15$	-3.59 ± 0.06	-0.95 ± 0.62
84812137	$2.92\text{e-}14\pm 2.97\text{e-}15$	-3.53 ± 0.06	-0.74 ± 0.94

Note: Column 1: spectral ID in LAMOST catalog. Column 2: unabsorbed flux in band 0.3–3.5 keV. Column 3: X-ray to optical flux ratio. Column 4: EPIC HR using the bands of 0.5–1 keV and 1–2 keV derived from 3XMM-DR5 catalog.

References

- Agüeros, M. A., Anderson, S. F., Covey, K. R., et al. 2009, *ApJS*, 181, 444
- Amôres, E. B., Robin, A. C., & Reylé, C. 2017, *A&A*, 602, A67
- Aurière, M., Konstantinova-Antova, R., Charbonnel, C., et al. 2015, *A&A*, 574, A90
- Baliunas, S., & Jastrow, R. 1990, *Nature*, 348, 520
- Brusa, M., Zamorani, G., Comastri, A., et al. 2007, *ApJS*, 172, 353
- Cardini, D., & Cassatella, A. 2007, *ApJ*, 666, 393
- Castelli, F., & Kurucz, R. L. 2004, arXiv:astro-ph/0405087
- Charbonneau, P. 2010, *Living Reviews in Solar Physics*, 7, 3
- Ciardi, D. R., von Braun, K., Bryden, G., et al. 2011, *AJ*, 141, 108
- Cui, X. Q., Zhao, Y. H., Chu, Y.Q., et al. 2012, *Research in Astronomy and Astrophysics*, 12, 1197
- Deng, L.-C., Newberg, H. J., Liu, C., et al. 2012, *Research in Astronomy and Astrophysics*, 12, 735

Table 2 Stellar parameters for the sample sources.

obsid	RA	DEC	subclass	V	A_V	Nh	T_{eff}	$\log(g)$	[Fe/H]
	(deg)	(deg)		(mag)	(mag)	(cm^{-2})	(K)		
(1)	(2)	(3)	(4)	(5)	(6)	(7)	(8)	(9)	(10)
1603040	9.873834	40.083248	G9	15.77±0.29	0.38	1.09e+21	5020.89±211.08	4.27±0.63	0.09±0.28
1615104	11.123160	41.359930	K1	14.17±0.03	1.12	3.22e+21	4808.98±106.97	3.05±0.58	-0.58±0.16
1615179	10.716530	41.518950	F6	15.81±0.01	1.31	3.77e+21	5280.53±322.29	3.04±1.17	-1.42±0.52
1615187	10.939620	41.616010	K3	15.34±0.08	0.64	1.82e+21	4872.15±256.63	3.42±0.61	-0.24±0.33
7003074	9.322592	40.763245	K5	15.25±0.05	0.23	6.54e+20	4491.66±88.32	4.22±0.26	-0.14±0.13
7003243	9.630176	40.286594	G8	15.70±0.07	0.30	8.58e+20	5141.44±194.22	4.08±0.54	-0.07±0.24
7711046	16.773656	32.182487	K5	15.02±0.05	0.19	5.32e+20	4464.46±121.34	4.01±0.30	0.10±0.16
20001189	185.349817	28.070038	K3	16.15±0.01	0.17	4.74e+20	4809.03±154.27	4.64±0.27	-0.04±0.23
28114180	98.454761	17.791983	G5	11.83±0.03	0.68	1.96e+21	5094.17±114.29	2.73±0.59	0.01±0.16
28306100	139.828255	30.428329	G3	12.63±0.05	0.07	2.09e+20	5728.46±166.85	4.41±0.52	-0.10±0.18
42815236	98.925573	5.526181	K0	11.61±0.14	0.89	2.55e+21	4745.80±54.52	2.69±0.52	-0.39±0.09
43810009	98.397596	17.657734	K4	14.40±0.04	1.88	5.38e+21	4599.58±120.03	1.82±0.57	-0.66±0.20
51007061	239.800512	27.268972	G3	11.75±0.01	0.20	5.81e+20	5821.85±122.08	4.06±0.56	0.06±0.13
53111238	235.942430	54.151718	F6	10.58±0.04	0.16	4.57e+20	6404.79±121.72	4.19±0.42	0.03±0.12
74309103	35.130959	-6.186942	F0	9.61±0.17	0.09	2.47e+20	6750.24±182.92	4.13±0.38	-0.04±0.18

Note: Column 1: spectral ID in LAMOST catalog. Column 2: right ascension. Column 3: declination. Column 4: stellar subclass. Column 5: V -band magnitude. Column 6: extinction in the V band. Column 7: hydrogen column density converted from optical extinction. Column 8: effective temperature. Column 9: surface gravity. Column 10: metallicity.

Durney, B. R., De Young, D. S., & Roxburgh, I. W. 1993, *Sol. Phys.*, 145, 207

Fekel, F. C. 1997, *PASP*, 109, 514

Foight, D. R., Güver, T., Özel, F., & Slane, P. O. 2016, *ApJ*, 826, 66

Georgakakis, A., Georgantopoulos, I., Vallbé, M., et al. 2004, *MNRAS*, 349, 135

Güdel, M. 2004, *A&A Rev.*, 12, 71

Harnden, F. R., Jr., Branduardi, G., Gorenstein, P., et al. 1979, *ApJ*, 234, L51

Henry, T. J., Soderblom, D. R., Donahue, R. A., & Baliunas, S. L. 1996, *AJ*, 111, 439

Houdebine, E. R., Mullan, D. J., Bercu, B., Paletou, F., & Gebran, M. 2017, *ApJ*, 837, 96

Hornschemeier, A. E., Bauer, F. E., Alexander, D. M., et al. 2003, *AJ*, 126, 575

Jansen, F., Lumb, D., Altieri, B., et al. 2001, *A&A*, 365, L1

Jardine, M., & Unruh, Y. C. 1999, *A&A*, 346, 883

Jeffries, R. D., Evans, P. A., Pye, J. P., & Briggs, K. R. 2006, *MNRAS*, 367, 781

Jenkins, J. S., Murgas, F., Rojo, P., et al. 2011, *A&A*, 531, A8

Table 3 Estimated parameters for the H α and H β lines.

obsid	subclass	EW _{Hα}	EW' _{Hα}	log($f_{\text{H}\alpha}/f_{\text{bol}}$)	FWHM _{Hβ,cor}	FWHM _{Hα,cor}
		(Å)	(Å)		(Å)	(Å)
(1)	(2)	(3)	(4)	(5)	(6)	(7)
1603040	G9	-0.44 ± 0.04
1615104	K1	-0.61 ± 0.03
1615179	F6	-1.67 ± 0.08
1615187	K3	-0.45 ± 0.45
7003074	K5	1.30 ± 0.22	1.93	-3.73 ± 0.05	...	1.26 ± 2.66
7003243	G8	-0.48 ± 0.06	3.42 ± 5.03	...
7711046	K5	0.78 ± 0.13
20001189	K3	-0.88 ± 0.12
28114180	G5	-1.31 ± 0.03
28306100	G3	-1.97 ± 0.04	1.84 ± 1.53	...
42815236	K0	-0.72 ± 0.03
43810009	K4	-0.81 ± 0.03
51007061	G3	-2.17 ± 0.05	2.28 ± 1.11	2.29 ± 1.07
53111238	F6	-2.56 ± 0.06	3.23 ± 0.83

Note: Column 1: spectral ID in LAMOST catalog. Column 2: stellar subclass. Column 3: H α EWs. Column 4: excess H α EWs. Column 5: H α to bolometric flux ratio. Column 6: corrected H β FWHMs. Column 7: corrected H α FWHMs.

Jester, S., Schneider, D. P., Richards, G. T., et al. 2005, *AJ*, 130, 873

Judge, P. G., Solomon, S. C., & Ayres, T. R. 2003, *ApJ*, 593, 534

Katsova, M. M., & Livshits, M. A. 2011, *Astronomy Reports*, 55, 1123

Krautter, J., Zickgraf, F.-J., Appenzeller, I., et al. 1999, *A&A*, 350, 743

Lin, D., Webb, N. A., & Barret, D. 2012, *ApJ*, 756, 27

Luo, A. L., Zhao, Y. H., Zhao, G., et al. 2015, *Research in Astronomy and Astrophysics*, 15, 1095

Luo, B., Bauer, F. E., Brandt, W. N., et al. 2008, *ApJS*, 179, 19-36

Maccacaro, T., Gioia, I. M., Wolter, A., Zamorani, G., & Stocke, J. T. 1988, *ApJ*, 326, 680

Mamajek, E. E., & Hillenbrand, L. A. 2008, *ApJ*, 687, 1264-1293

Martínez-Arnáiz, R., López-Santiago, J., Crespo-Chacón, I., & Montes, D. 2011, *MNRAS*, 414, 2629

Noyes, R. W., Hartmann, L. W., Baliunas, S. L., Duncan, D. K., & Vaughan, A. H. 1984, *ApJ*, 279, 763

Özdarcan, O., & Dal, H. A. 2018, arXiv:1801.06087

Pace, G. 2013, *A&A*, 551, L8

- Pallavicini, R., Golub, L., Rosner, R., et al. 1981, *ApJ*, 248, 279
- Pizzolato, N., Maggio, A., Micela, G., Sciortino, S., & Ventura, P. 2003, *A&A*, 397, 147
- Prosser, C. F., Randich, S., Stauffer, J. R., Schmitt, J. H. M. M., & Simon, T. 1996, *AJ*, 112, 1570
- Reid, I. N., Hawley, S. L., & Gizis, J. E. 1995, *AJ*, 110, 1838
- Reiners, A., Schüssler, M., & Passegger, V. M. 2014, *ApJ*, 794, 144
- Rocha-Pinto, H. J., & Maciel, W. J. 1998, *MNRAS*, 298, 332
- Rogel, A. B., Lugger, P. M., Cohn, H. N., et al. 2006, *ApJS*, 163, 160
- Rosen, S. R., Webb, N. A., Watson, M. G., et al. 2016, *A&A*, 590, 1
- Schlafly, E. F., & Finkbeiner, D. P. 2011, *ApJ*, 737, 103
- Schmitt, J. H. M. M., Collura, A., Sciortino, S., et al. 1990, *ApJ*, 365, 704
- Schmitt, J. H. M. M., Fleming, T. A., & Giampapa, M. S. 1995, *ApJ*, 450, 392
- Schmitt, J. H. M. M. 1997, *A&A*, 318, 215
- Schrijver, C. J., Mewe, R., & Walter, F. M. 1984, *A&A*, 138, 258
- Schröder, C., & Schmitt, J. H. M. M. 2007, *A&A*, 475, 677
- Skumanich, A. 1972, *ApJ*, 171, 565
- Simon, T., & Drake, S. A. 1989, *ApJ*, 346, 303
- Simon, T., Herbig, G., & Boesgaard, A. M. 1985, *ApJ*, 293, 551
- Sissa, E., Gratton, R., Desidera, S., et al. 2016, *A&A*, 596, A76
- Solanki, S. K., Motamen, S., & Keppens, R. 1997, *A&A*, 325, 1039
- Stelzer, B., Marino, A., Micela, G., López-Santiago, J., & Liefke, C. 2013, *MNRAS*, 431, 2063
- Stocke, J. T., Liebert, J., Gioia, I. M., et al. 1983, *ApJ*, 273, 458
- Stocke, J. T., Morris, S. L., Gioia, I. M., et al. 1991, *ApJS*, 76, 813
- Strassmeier, K. G., Fekel, F. C., Bopp, B. W., Dempsey, R. C., & Henry, G. W. 1990, *ApJS*, 72, 191
- Telleschi, A., Güdel, M., Briggs, K., et al. 2005, *ApJ*, 622, 653
- Telleschi, A., Güdel, M., Briggs, K. R., Audard, M., & Palla, F. 2007, *A&A*, 468, 425
- Testa, P., Saar, S. H., & Drake, J. J. 2015, *Philosophical Transactions of the Royal Society of London Series A*, 373, 20140259
- Vaiana, G. S. 1983, *Solar and Stellar Magnetic Fields: Origins and Coronal Effects*, 102, 165
- Vaughan, A. H., & Preston, G. W. 1980, *PASP*, 92, 385
- Vilhu, O. 1984, *A&A*, 133, 117
- Vilhu, O., & Walter, F. M. 1987, *ApJ*, 321, 958
- Voges, W., Aschenbach, B., Boller, T., et al. 1999, *A&A*, 349, 389
- Walter, F. M., & Bowyer, S. 1981, *ApJ*, 245, 671
- Wegner, W. 2007, *MNRAS*, 374, 1549
- Wright, J. T., Marcy, G. W., Butler, R. P., & Vogt, S. S. 2004, *ApJS*, 152, 261
- Wright, N. J., Drake, J. J., Mamajek, E. E., & Henry, G. W. 2011, *ApJ*, 743, 48
- Wilson, O. C. 1963, *ApJ*, 138, 832
- Worthey, G., Faber, S. M., Gonzalez, J. J., & Burstein, D. 1994, *ApJS*, 94, 687

- Wu, Y., Luo, A.-L., Li, H.-N., et al. 2011, *Research in Astronomy and Astrophysics*, 11, 924
- Xiang, M.-S., Liu, X.-W., Shi, J.-R., et al. 2017, *MNRAS*, 464, 3657
- Yang, H., Liu, J., Gao, Q., et al. 2017, *ApJ*, 849, 36
- Zacharias, N., Finch, C. T., Girard, T. M., et al. 2013, *AJ*, 145, 44
- Zhao, G., Zhao, Y. H., Chu, Y. Q., et al. 2012, *Research in Astronomy and Astrophysics*, 12, 723
- Zickgraf, F.-J., Engels, D., Hagen, H.-J., Reimers, D., & Voges, W. 2003, *A&A*, 406, 535